Nearly triple nodal point topological phase in half-metallic GdN

Jinwoong Kim, Heung-Sik Kim, and David Vanderbilt[*]
Department of Physics & Astronomy, Rutgers University, Piscataway, New Jersey 08854, USA

(Received 30 July 2018; published 12 October 2018)

Recent developments in topological semimetals open a way to realize relativistic dispersions in condensed-matter systems. One recently studied type of topological feature is the "triple nodal point" where three bands become degenerate. In contrast to Weyl and Dirac nodes, triple nodal points, which are protected by a rotational symmetry, have nodal lines attached, so that a characterization in terms of a chirality is not possible. Previous studies of triple nodal points considered nonmagnetic systems, although an artificial Zeeman splitting was used to probe the topological nature. Here instead we treat a ferromagnetic material, half-metallic GdN, where the splitting of the triple nodal points comes from the spin-orbit coupling. The size of the splitting ranges from 15 to 150 meV depending on the magnetization orientation, enabling a transition between a Weyl-point phase and a "nearly triple nodal point" phase that exhibits very similar surface spectra and transport properties compared with a true triple-node system. The rich topological surface states, manipulable via the orientation of the magnetization, make half-metallic GdN a promising platform for future investigations and applications.

DOI: 10.1103/PhysRevB.98.155122

I. INTRODUCTION

In the last decade, an enormous expansion in studies of topological materials has opened a powerful new perspective in materials science [1–5]. While topological insulators are classified by integer Chern numbers or Z_2 indices [1–4], topological semimetals [6–8] may be characterized by the type of low-energy excitations they admit, in analogy with the description of elementary particles in high-energy physics. In particular, the excitations near a Dirac or Weyl point in a topological semimetal behave similarly to the massless Dirac and Weyl fermions that arise in the quantum field theory of elementary particles. A Dirac point corresponds to a point fourfold degeneracy resulting from a crossing of twofold degenerate bands in momentum space; since the Berry flux surrounding such a point vanishes, it has no net chirality. By contrast, a Weyl point results from a crossing of just two bands, and depending on its chirality, either emits or absorbs a 2π quantum of Berry flux. As a consequence, Fermi arc states emerge in the surface Brillouin zone (BZ) connecting the projected locations of the Weyl points.

A recently studied threefold band-crossing point, referred to as a triple nodal point (TNP), is protected by a crystalline (typically C_3 rotation) symmetry [9–15]. In contrast to the case of Dirac and Weyl points, the Berry phase of the TNP is ill-defined due to the inevitable presence of nodal lines attached to the TNP, which prohibits the occurrence of a gapped surface enclosing a single TNP. Although the formation of surface states has been demonstrated for several TNP materials, the identification of a general feature expected in the surface states, analogous to the Fermi arc states, has remained elusive. Moreover, the surface-state features are likely to be obscured if more than one TNP projects to the same point on the cleavage surface; this commonly occurs if that surface is orthogonal to the primary rotation axis, which is the case in most of the suggested TNP metals proposed to date [9–14].

Here, we focus instead on half-metallic GdN possessing three perpendicular C_4 rotational axes so that at least two pairs of TNPs are exposed on a surface. GdN and most of the rare-earth monopnictide compounds occur in the rocksalt structure and exhibit a variety of magnetic and transport properties [16,17]. Early systematic theoretical studies [18–20] on the rare-earth nitrides found a range of electronic structures from narrow-gap insulators (TbN, DyN, HoN) to half-metallic ferromagnets (PrN, NdN, PmN, SmN, EuN, GdN) and ordinary metallic ferromagnetic materials (CeN, ErN, TmN, YbN). Among the half-metallic ferromagnets, GdN exhibits the highest Curie temperature (T_C) of 58 K [21] and is reported to be a Chern insulator in an ultrathin two-dimensional layer form [22], suggesting that potential Weyl nodes might emerge in the three-dimensional BZ [23]. Although its exact band gap is still under debate even after intense study [18,24–30], there have been consistent reports that the band gap decreases upon magnetic ordering below T_C [29,31], external pressure [25,32,33], and external magnetic fields [26].

In view of the similarity of the electronic structure and the tunability of the band gaps in rare-earth monopnictides, we have chosen to focus here on GdN as a representative material for in-depth study. We find that GdN exhibits a "nearly triple nodal point" (NTNP) topological phase, analogous to the TNP phase but with a very small lifting of the degeneracy of the TNPs. The NTNPs come in pairs centered on the three X points in the BZ. Because the spin-orbit coupling (SOC) is so weak on N, while the spin splitting of the Gd orbitals is so large that the Gd SOC is largely quenched, the SOC-induced splitting at each of the NTNPs is quite small. In fact, the system is characterized by the presence of several distinct energy scales, with the hopping-controlled bandwidth

---

[*] dhv@rutgers.edu

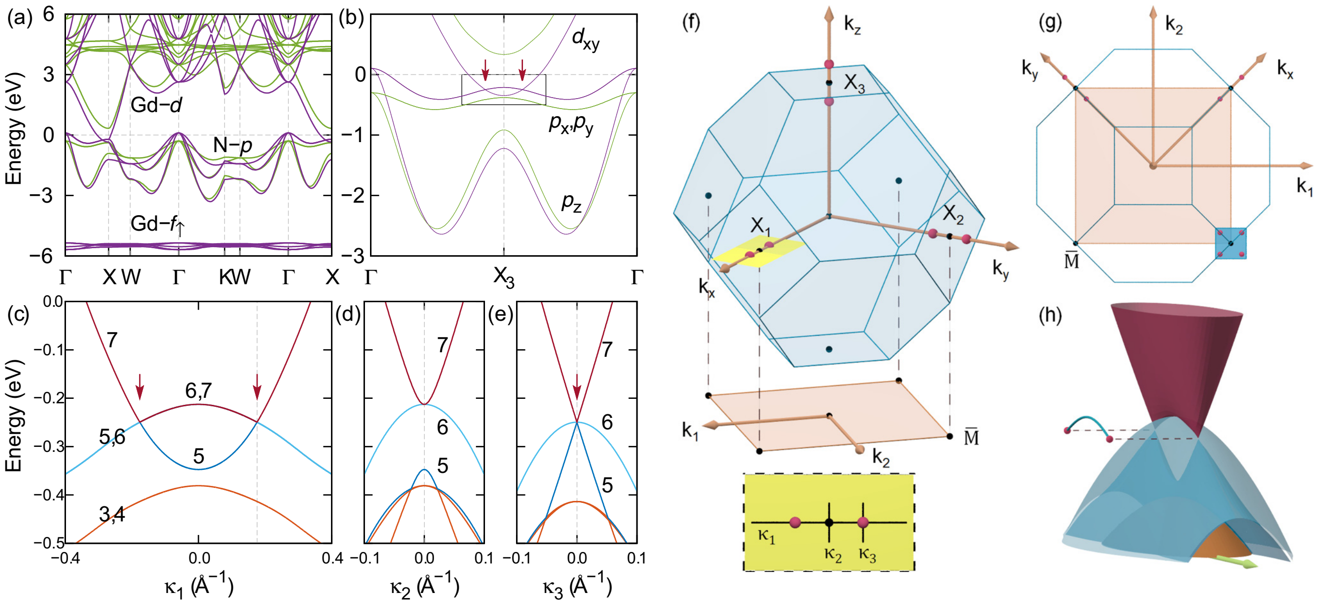

FIG. 1. (a)–(e) Band structure of GdN calculated without SOC. (a), (b) The purple (green) colors represent spin majority (minority) bands, while in the blow-ups in panels (c)–(e) the colors are keyed to indicated band index numbers, where band 6 is the highest valence band. Triple nodal points are marked with red arrows. (f) Relation of the bulk Brillouin zone (BZ) to the two-dimensional (2D) projected BZ on the (001) surface. Six red dots denote triple nodal points; yellow rectangle defines the three variables κ_1, κ_2, and κ_3 used as the horizontal axes in panels (c)–(e). (g) Top view of the BZ, showing the overlap between bulk and surface BZs. Blue square is the area used for constant-energy scans in Figs. 2 and 4–6. (h) 2D band structure plotted on the $k_z = 0$ plane near the X_1 point; the arrow at the base is directed toward the Γ point, and the shifted blue line terminating in two dots illustrates the nodal line connecting the two triple nodal points.

dominating the exchange splitting which in turn is much larger than the SOC, leading to a complex electronic structure.

Because the splitting of the TNP is so weak, the NTNP phase is found to have qualitatively similar surface spectra and transport properties compared to a true TNP phase. Interestingly, depending on the magnetic-moment orientation, some of the NTNPs decompose into conventional Weyl points. As a result, we predict that a selected rotation of the magnetization with external field can drive transitions between Weyl and NTNP behavior in selected nodal regions, with associated transitions in the surface-state topology.

II. METHODOLOGY

To investigate the electronic properties of GdN, *ab initio* calculations are carried out by using VASP and wannierized by using the VASP-WANNIER90 interface [34–36] to arrive at a tight-binding description of first-principles quality. The pseudopotential is of the projector-augmented-wave type [37] as implemented in VASP [38]. The generalized gradient approximation exchange-correlation functional is employed as parametrized by Perdew, Burke, and Ernzerhof [39] with a Coulomb U of 4.5 eV on the Gd f orbits. The plane-wave basis is expanded up to the cutoff energy of 400 eV and $12 \times 12 \times 12$ k-mesh grid is used in the VASP calculations. Six N p and ten Gd d atomic orbitals are projected for the Wannier representation with spin polarization but without SOC. The atomic SOC is then included in the tight-binding Hamiltonian. The surface states for a semi-infinite geometry are calculated by employing an iterative surface Green's function method [40,41]. Landau-level spectra are calculated by using a symmetry-constraint $\boldsymbol{k}\cdot\boldsymbol{p}$ model with Peierls substitution [42,43].

III. RESULTS AND DISCUSSION

A. Without spin-orbit coupling

The electronic structure of GdN in the absence of SOC is shown in Fig. 1. Near the Fermi level, the valence and conduction bands mostly consist of N p and Gd t_{2g} orbitals, respectively. In the nonmagnetic phase, a small indirect gap appears between the Γ and X points. When cooled down below the Curie temperature of 58 K [21], GdN becomes half metallic due to the opposite sign of the Zeeman splitting on Gd and N atoms, causing a band inversion only in the majority-spin channel. The band inversion does not open a mass gap because the bands belong to different irreps of the C_4 rotations about the primary Γ–X axes. For example, concerning C_4 rotations about the z axis, the states on the Γ–X_3 line obey $R(C_4^{\hat{z}})|d_{xy}\rangle = -1|d_{xy}\rangle$ and $R(C_4^{\hat{z}})|p_x \pm ip_y\rangle = \pm i|p_x \pm ip_y\rangle$. Note that the $|p_x \pm ip_y\rangle$ valence-band states remain doubly degenerate, since in the absence of SOC the orbital moment does not couple with the spin moment. The crossing point is thus triply degenerate and is referred to as a TNP [12–15,44].

Figures 1(c) and 1(h) show that each pair of TNPs near an X point is connected by a nodal line. Since a cross section of the nodal line is a quadratic touching point [Fig. 1(d)], the Berry phase around the nodal line is zero and no surface state is induced by the nodal line [13,14]. In the notation of Refs. [13,14], this corresponds to a type-A TNP. (Their type-B TNP is connected by several nodal lines lying off the

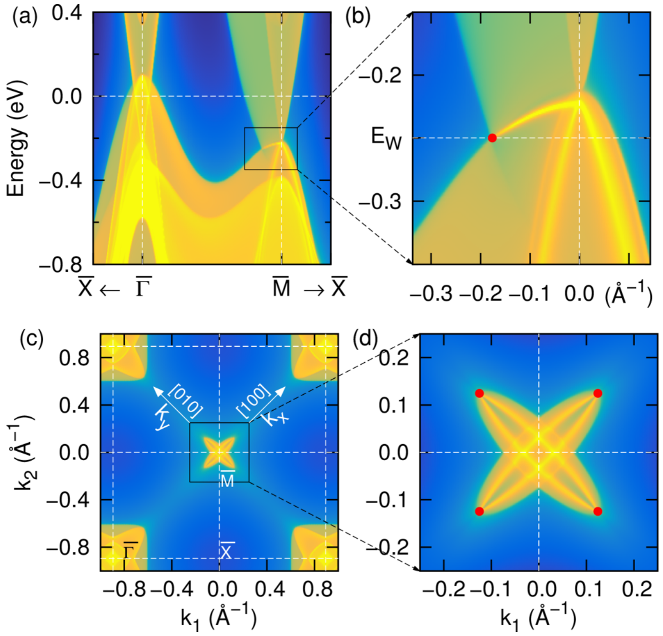

FIG. 2. Surface states on the (001) surface calculated for a semi-infinite geometry without SOC. (a), (b) Surface band spectral function. (c), (d) Constant-energy scan at $E = E_W$. Bright (dim) yellow color represents surface (bulk) state. The origin has been shifted to the $\overline{M}$ point. Panels (b) and (d) are zoomed in around the $\overline{M}$ point; red dots indicate triple nodal points.

symmetry axis in addition to the one lying on the axis.) In contrast to the typical TNP materials, the TNPs of GdN are protected by C_4 rotational symmetry in the absence of SOC.[1]

Unlike Weyl points and nodal loops, which generate Fermi arcs and drumhead states, respectively, previous work has not identified a corresponding general feature expected in the surface-state spectrum of a TNP material. In comparison with previously reported TNP materials, the TNPs of GdN are sufficiently well isolated from irrelevant bands that the resulting surface states can be well characterized.

Figure 2 shows the surface states of semi-infinite GdN in the absence of SOC. The right panels are blowups of the left panels, with the TNPs shown as red dots. Figures 2(c) and 2(d) are constant-energy intensity plots on a plane containing four TNPs, at the energy of the TNPs. The surface states attributed to the TNPs appear bright yellow in Figs. 2(b) and 2(d), in comparison with the dim bulk states in dark yellow. In Fig. 2(d), the projected TNPs are clearly seen to be attached by two branches of Fermi arcs. Overall, the surface-state structure looks like two overlapping copies of an elliptical dome rotated by 90° with respect to each other. The shape of the surface-state structure is discussed and further illustrated in Sec. III C. These elliptical domes, which have open sides below the two TNPs, are detached from the conduction band, contrary to the case of the surface states of a conventional Weyl phase. The dome shape can be understood as a hybridization of two surface states individually induced by two pairs of conventional Weyl points, as will be discussed in more detail below.

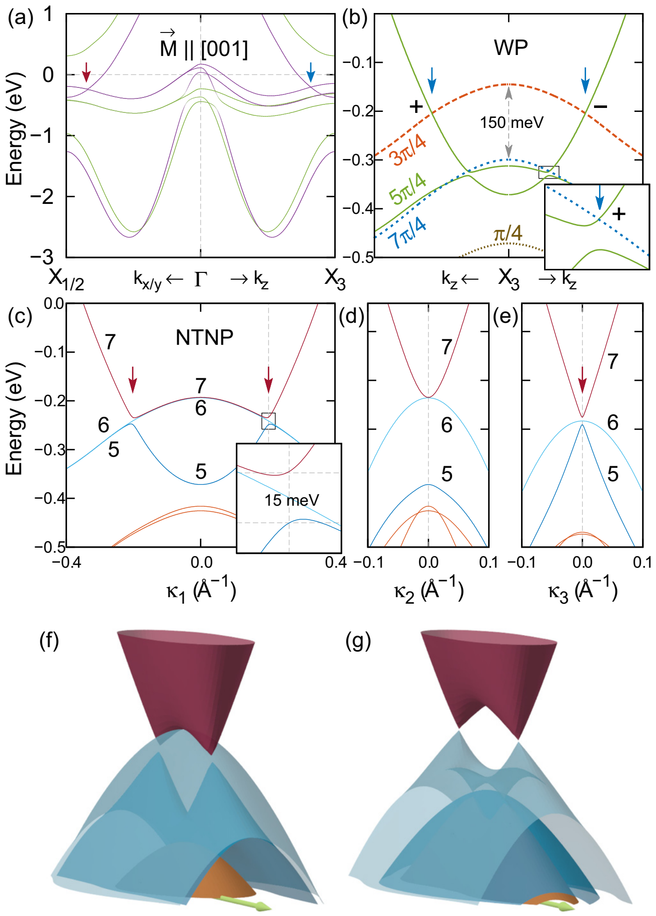

FIG. 3. Electronic structure of GdN calculated with SOC. The magnetic moment is aligned along the [001] direction. (a) Band dispersion along the three Cartesian axes. The purple (green) colors represent spin majority (minority) bands. (b) Band structure on the k_z axis, where band labels denote eigenvalues of the $C_4^{\hat{z}}$ operator. (c)–(e) Band structure on κ_1, κ_2, and κ_3 lines. Blue and red arrows denote Weyl and nearly triple nodal points, respectively. (f), (g) 2D band structure on k_x–k_y and k_z–k_x planes at X_1 and X_3, respectively. The arrows at the base are directed toward the Γ point.

B. With spin-orbit coupling

When taking SOC into account, a direction of the net magnetic moment has to be specified. If we take it along the [001] direction, the degeneracy of the $|p_x \pm ip_y\rangle$ valence bands on the k_z axis is significantly lifted, whereas the corresponding states on the k_x and k_y axes are hardly altered, as shown in Fig. 3. On the k_x axis, for instance, the band of $|p_x\rangle$ character is more dispersive and located lower in energy than the $|p_y\rangle$ and $|p_z\rangle$ bands, due to stronger orbital overlaps along the $\hat{x}$ direction. The large energy separation of $|p_x\rangle$ and $|p_y\rangle$ bands causes a weak coupling with the magnetic moment $\boldsymbol{M} \parallel [001]$. As will be discussed below, the resulting

---

[1] Note that C_4 symmetry cannot protect TNPs in the presence of SOC. If time reversal is absent, there are only one-dimensional irreps, and their crossings generate simple Weyl points. If it is present, irreps $\theta = \pm\pi/4$ and $\pm 3\pi/4$ come in time-reversal pairs, enforcing every crossing on the C_4 axis to be fourfold degenerate. See also Ref. [44].

surface states are quantitatively similar to those of the true TNP phase, as manifested by turning off the SOC. Therefore, we refer to the nearly triply degenerate crossing points as “nearly triple nodal points” (NTNPs). Figures 3(c)–3(f) show the zoomed-in band dispersion of the NTNPs corresponding to Figs. 1(c)–1(e) and 1(h), respectively. The NTNPs have a small gap opening of ∼15 meV.

When SOC is introduced, the C_4 rotational symmetries are generally broken in the presence of a magnetic moment that is not parallel to the rotation axis. However, with the parallel magnetic moment $\boldsymbol{M} \parallel [001]$, $C_4^{\hat{z}}$ symmetry still remains and Bloch states on the k_z axis are classified with the eigenvalues of the rotational operator, $R(C_4^{\hat{z}})$. Figure 3(b) shows the band structure labeled by the phase $\theta = \{\frac{\pi}{4}, \frac{3\pi}{4}, \frac{5\pi}{4}, \frac{7\pi}{4}\}$ of the eigenvalues of the $C_4^{\hat{z}}$ operator. The two bands having the same phase $\theta = 5\pi/4$ mix with each other and open a mass gap, whereas others with distinct phases cross each other without a gap opening, producing a conventional twofold Weyl node. The Chern number of a Weyl point can be determined by the phase difference of the two crossing bands [45,46]. For example, the point at which a $\theta = 3\pi/4$ band crosses up (down) through a $\theta = 5\pi/4$ band with increasing z has a Chern number of $+1$ (-1), and would serve as the terminus for a single Fermi arc on the surface. The other crossing points between $\theta = 5\pi/4$ and $\theta = 7\pi/4$ bands produce another pair of Weyl points, of which one is shown in the inset with a Chern number of $+1$. The two-dimensional (2D) band structure in Fig. 3(g) shows that the parabolic band is shifted down in energy due to the Zeeman splitting, leaving two conventional Weyl nodes prominently exposed. Since the Weyl points are robust unless they are mutually annihilated, the Weyl points still survive under a small rotation of the magnetic moments even without the $C_4^{\hat{z}}$ symmetry. Under the rotation, the Weyl points are found to migrate in the vicinity of the primary axis (not shown here).

C. Manipulation via magnetization and strain

It is important to note that the NTNPs appear on the axes perpendicular to the magnetic-moment direction, while the Weyl points lie on the parallel axis. Thus, if one rotates the magnetic moment from $\boldsymbol{M} \parallel [001]$ toward the [100] direction (keeping $M_y = 0$), the NTNPs on the k_y axis are unaffected, whereas those on the k_x axis split into Weyl points because the degeneracy of the $|p_y \pm i p_z\rangle$ valence-band states is lifted by the finite M_x.

Because the magnetocrystalline anisotropy of GdN is very small,[2] one can easily control the magnetization orientation by applying an external magnetic field. In cooperation with the SOC, the magnetic moment of GdN is thus a tool that can be used to manipulate the Weyl nodes in energy and momentum space, and thus the surface states as well. The calculated semi-infinite (001) surface states are shown in Figs. 4–6 with respect to the magnetic-moment orientation. For a magnetic moment normal to the surface, two pairs of NTNPs are projected on the surface BZ and connected by elliptical dome-like surface states as illustrated in Fig. 4(c). This surface state has similar features as that of the true TNP phase presented above in the absence of the SOC [Figs. 2(b) and 2(d)].

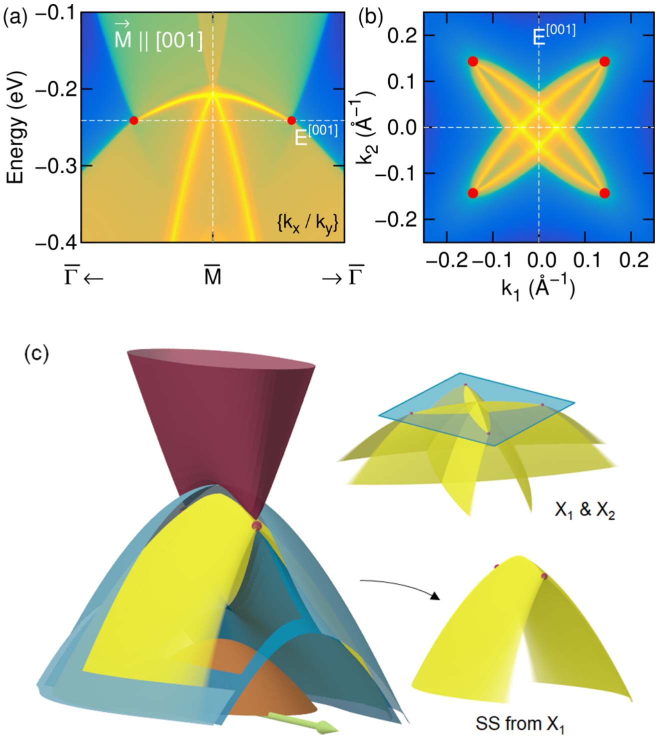

FIG. 4. Electronic structure on the (001) surface calculated for a semi-infinite geometry with the magnetization orientation of [001] direction. (a) Band structure at the $\bar{M}$ point. (b) Constant-energy scan at $E = E^{[001]}$. Bright yellow color denotes intense spectral density. (c) Schematic view of the nearly triple-nodal-point surface state emerging from the X_1 and X_2 points. Red dots are nearly triple nodal points.

A magnetic moment along the [110] direction makes the four NTNPs split into four pairs of conventional Weyl points (Fig. 5). This is different from the splitting of a Dirac point into two Weyl points, in that here one Weyl point is located one band index higher than the other Weyl point. For instance, four Weyl points are crossings of valence and conduction bands (at an energy level of $E_1^{[110]}$) while the other four Weyl points are crossings of two valence bands (at an energy level of $E_2^{[110]}$). Figure 5(d) shows two Fermi arcs connecting two pairs of Weyl points on the constant-energy plane $E = E_1^{[110]}$. Since the Weyl points are crossings of valence and conduction bands, the surface states are guaranteed to connect valence and conduction bands crossing the energy gap at $E_1^{[110]}$ [Figs. 5(a)–5(c)]. Surface states from the other four Weyl points on $E = E_2^{[110]}$ are immersed in the bulk valence bands as marked by an arrow in Fig. 5(b). Nevertheless, the constant-energy plot [Fig. 5(e)] still shows embedded Fermi arcs connecting the Weyl nodes. An arrow in Fig. 5(c) shows a small gap at the crossing points, implying a finite interaction between the two Fermi arcs.

---

[2] According to our calculations, the total energy is equal within numerical accuracy for magnetization along [110] or [111], and only about 0.05 meV per formula unit higher for magnetization along [100].

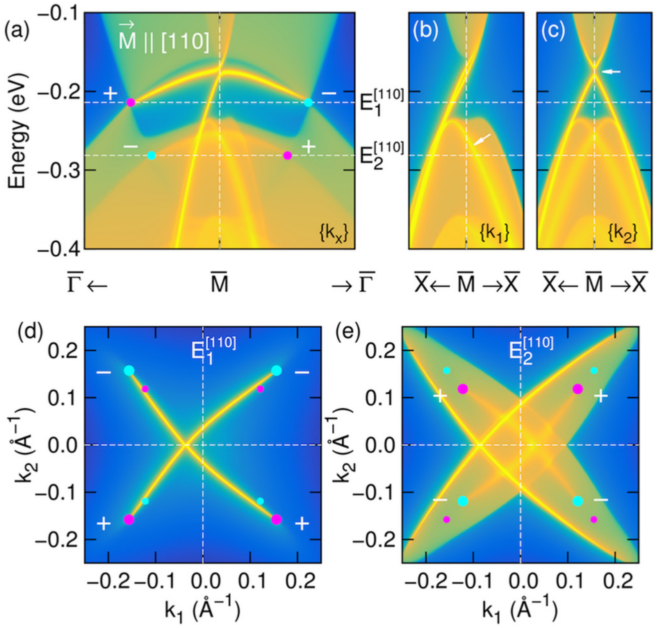

FIG. 5. Electronic structure on the (001) surface calculated for a semi-infinite geometry with the magnetization along the [110] direction. (a)–(c) Band structure at the $\bar{M}$ point along k_x, k_1, and k_2 directions [see Fig. 1(g)]. Constant-energy-scans at (d) $E = E_1^{[110]}$ and (e) $E = E_2^{[110]}$. Magenta (cyan) dots denote the position of Weyl points with positive (negative) chirality. In panels (d) and (e), large dots lie on the energy plane of the plot, while small dots lie off the plane.

The last case we discuss here is when the magnetic moment is aligned along the [100] direction, which lifts the NTNPs on the k_x axis but not on the k_y axis as shown in Figs. 6(a) and 6(b), respectively. The Fermi arcs at relevant energy levels are plotted in Figs. 6(e)–6(h), showing the coexistence of the NTNP and the conventional Weyl point phase. It is noteworthy that the Fermi arc is tangentially attached to the hole or electron pockets enclosing the Weyl points, as is clearly demonstrated in Fig. 6(e). This is expected based on the analysis of Haldane [47], but to our knowledge this has not previously been demonstrated by using *ab initio* calculations. If the energy is decreased so that it falls below the Weyl point, the Fermi arc becomes attached to the other side of the hole pocket [Fig. 6(g)], preserving the tangential attachment, in good agreement with the prediction [47].

Figure 6(i) illustrates the surface states of a cubic crystallite of GdN, showing that the surfaces parallel to the magnetic-moment direction have chiral conducting channels associated with the bulk Weyl nodes. These chiral channels circulate in a right-handed manner relative to the magnetic-moment direction. This is true not only for $\boldsymbol{M} \parallel [100]$, but also for an arbitrary direction of $\boldsymbol{M}$, because the component of the Weyl-point chiral dipole moment is proportional to the magnetization in each Cartesian direction. Figure 7 shows that, in the simplest case of $\boldsymbol{M} \parallel [100]$, only one pair of Weyl points lies on the k_x axis in the vicinity of the Fermi level, giving nonzero anomalous Hall conductivity σ_{yz}. Figure 7(c) shows the partial Chern numbers $\mathcal{Z}$, where

$$\sigma_{yz}(k_x) = -\frac{e^2}{h}\mathcal{Z}(k_x), \tag{1}$$

calculated in 2D (k_y, k_z) momentum space as a function of k_x for two chemical potentials. It shows plateaus in gapped windows of k_x where σ_{yz} is well quantized to either 0 or −1, corresponding to the region between the two Weyl points

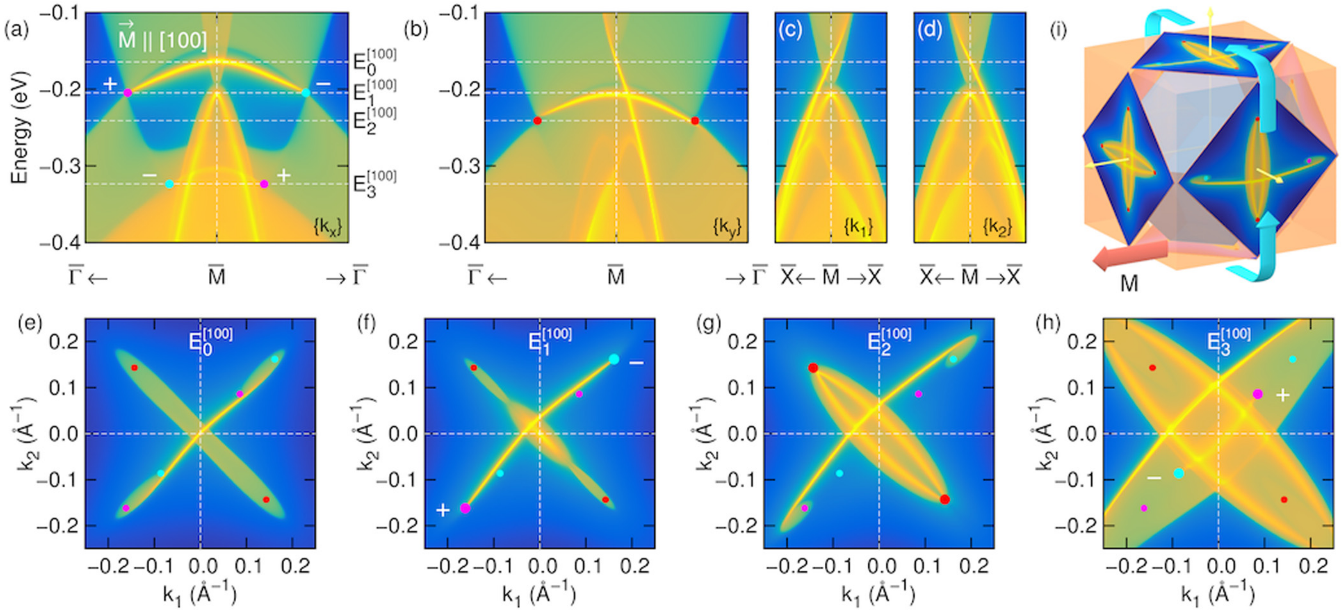

FIG. 6. Electronic structure of the (001) surface calculated for a semi-infinite geometry with the magnetization along the [100] direction. (a)–(d) Band structure at the $\bar{M}$ point along k_x, k_y, k_1, and k_2 directions. Constant-energy scans at (e) $E = E_0^{[100]}$, (f) $E = E_1^{[100]}$, (g) $E = E_2^{[100]}$, and (h) $E = E_3^{[100]}$. Red dots represent nearly triple nodal points. Magenta (cyan) dots denote Weyl points with positive (negative) chirality. In panels (e)–(h), large dots lie on the energy plane of the plot, while small dots lie off the plane. (i) Schematic view of the chiral surface states. Red and blue arrows indicate direction of magnetization and surface group velocity, respectively.

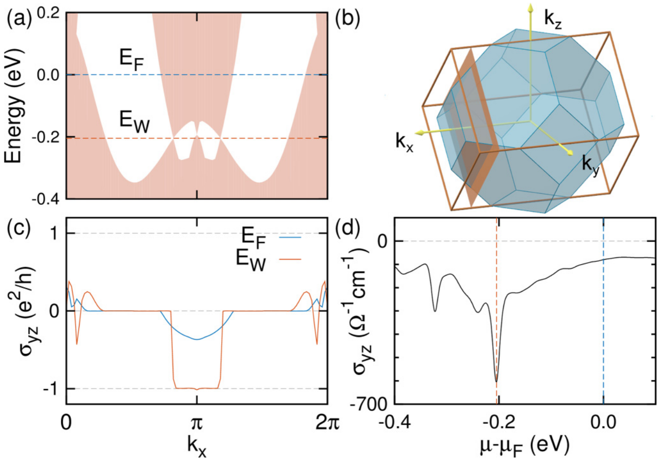

FIG. 7. Anomalous Hall conductivity for magnetization along the [100] direction. (a) Electronic states projected on the k_x axis from the tetragonal Brillouin zone (BZ) having the same volume as the conventional Wigner–Seitz BZ, as shown in panel (b). (c) Two-dimensional anomalous Hall conductivity vs k_x calculated on constant-k_x planes, one of which is shown as a colored square in panel (b), including all states below E_F (blue) or E_W (brown). (d) Bulk anomalous Hall conductivity as a function of chemical potential.

associated with the surface chiral channels. Unfortunately, the Weyl points are separated from the Fermi level by about −0.2 eV, suggesting that gating or doping would be required to measure the chiral transport properties shown in Fig. 7(d).

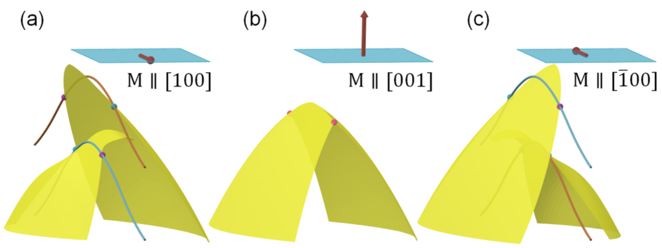

FIG. 8. Schematic view of the GdN surface-state transition on the (001) surface for magnetization orientation along (a) [100], (b) [001], and (c) $[\bar{1}00]$. Orange and blue lines represent two bulk bands on the k_x axis having $C_4^{\hat{x}}$ eigenvalues of $\exp(i3\pi/4)$ and $\exp(i7\pi/4)$, respectively [see Fig. 3(b)].

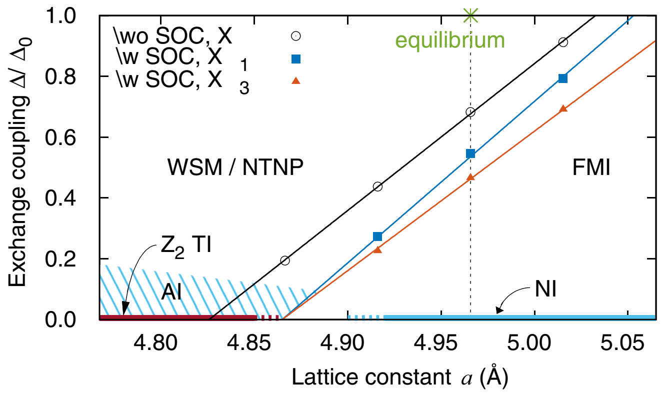

FIG. 9. Topological phase diagram of GdN as a function of strain and exchange coupling with the magnetic moment along [001]. Plotted lines indicate closures of the direct band gap: without SOC (black), simultaneously at all three X points; and with SOC, at X_1 (blue) and X_3 (red). Vertical dashed line indicates the equilibrium lattice constant. Acronyms are WSM for Weyl semimetal, NTNP for nearly triple nodal point, FMI for ferromagnetic insulator, TI for topological insulator, AI for axion insulator, and NI for normal insulator.

The dome-like surface state of the NTNP phase can be understood as a transitional state between the two Weyl phases. This is illustrated in Fig. 8, which shows the topological surface state on the (001) surface induced by Weyl points or NTNPs on the k_x axis. When rotating the magnetic moment from the [100] to the [001] direction, two initially separated valence bands become nearly degenerate, inducing a pair of NTNPs. A further rotation to the $[\bar{1}00]$ direction splits the two valence bands again, in such a way that the chirality is exchanged and the surface states acquire the opposite group velocities. Note that an external magnetic field will also split TNPs into Weyl nodes [13], and the rotation of the applied field can cause a qualitatively similar transition in the TNP surface states. Thus, the TNP and NTNP phases act as intermediate neutral states at which the chirality is reversed via the fusion and fission of two chiral surface states.

An essential prerequisite for the occurrence of the band crossings that we have analyzed above is the presence of a band inversion at the X points, which is quite sensitive to the lattice constant and to the exchange-coupling strength. Figure 9 shows the calculated location of the band-gap closure as a function of these two parameters. We find that both compressive strain and stronger exchange coupling enhance the band inversion, in agreement with previous reports [25,26,29,31–33]. The SOC also strengthens the band inversion, especially on the primary axis parallel to the magnetic moment, due to its larger band splitting. Therefore, in the region between the blue and red lines, GdN has only one pair of Weyl points. It is noteworthy that a uniaxial pressure may widen the single-pair area by causing compressive and tensile strains along the X_3 and $X_{1,2}$ axes respectively, as will be discussed below. Once all three band inversions have occurred, the number of NTNP is determined by the magnetic moment direction. If the magnetic moment disappears at $T > T_C$, the C_4-rotational and time-reversal symmetries are recovered together with the spin degeneracy of each band. On the Cartesian axes, the spin-degenerate valence and conduction bands near the Fermi level have C_4 eigenvalues of $\theta = \pm 3\pi/4$, implying a mass gap where they cross. The band inversion at the three X points implies that the topology of the bands lying below the global direct gap is that of a Z_2 time-reversal topological insulator, and if a weak ordering of the magnetic moments is turned on, this turns into an axion insulating phase in a narrow window of the exchange coupling parameter labeled as “AI” in Fig. 9.

The fact that the three band inversions occur on three orthogonal primary axes opens the possibility of tuning these gaps individually via anisotropic strains. A uniaxial compressive stress, for instance, should enhance the band inversion on the primary axis while reducing or eliminating it on the other two axes. Thus, this might result in just a single band

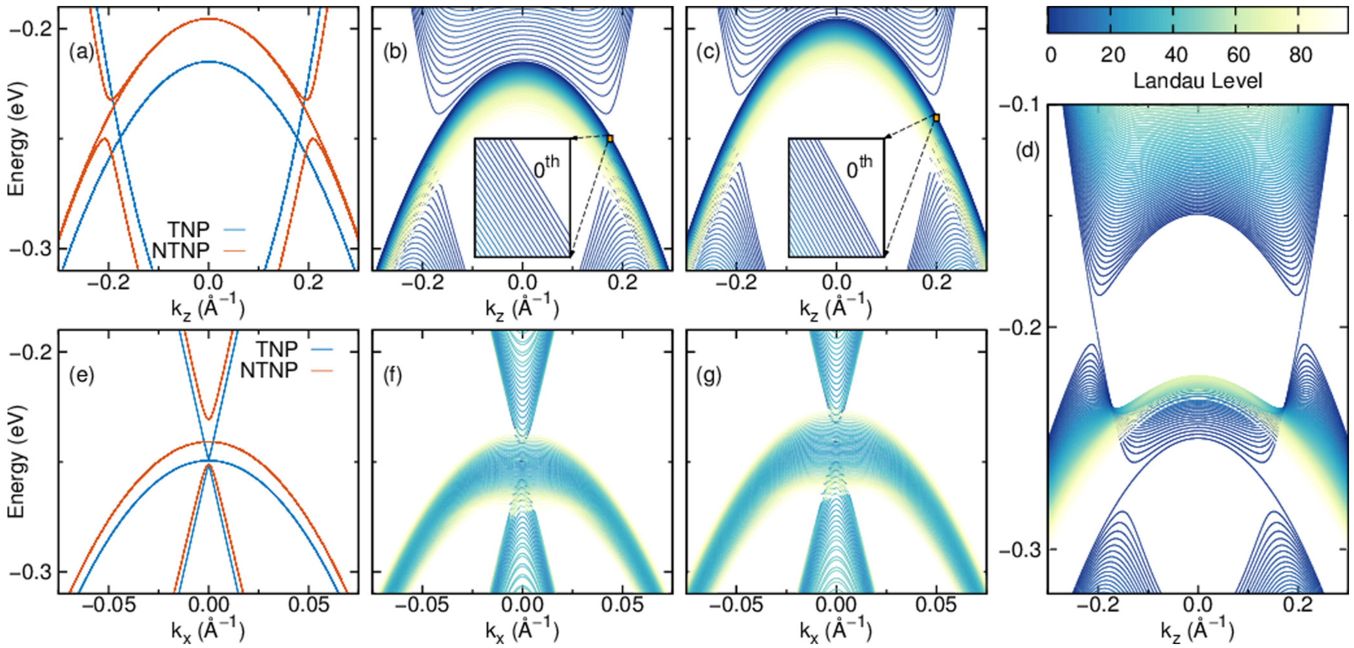

FIG. 10. Landau-level spectra of GdN calculated with the $\boldsymbol{k}\cdot\boldsymbol{p}$ model. (a), (e) Band structure calculated with the $\boldsymbol{k}\cdot\boldsymbol{p}$ model along k_z and k_x directions, respectively. (b), (c) Landau-level spectra along k_z axis for triple nodal point and nearly triple nodal point phases, respectively. (d) Landau-level spectra along the k_z axis for the Weyl semimetal phase. (f), (g) Landau-level spectra along the k_x direction for the triple nodal point and nearly triple nodal point phases, respectively. Dark blue color in panels (b)–(d) and (f), (g) indicates low-index Landau levels [see color bar in panel (d)].

inversion, with one pair of NTNPs or one pair of Weyl points (depending on magnetization direction) on the primary axis. A biaxial stress might induce two pairs of Weyl points without any NTNPs. It is worth recalling that the effective degeneracy on the k_x axis originates from N p_y and p_z orbitals and is lifted by distinct lattice constants $a_y \neq a_z$. Under biaxial pressure, therefore, the NTNPs cannot emerge on the two in-plane axes, regardless of the magnetic-moment direction.

D. Landau-level spectra

One characteristic feature of a TNP material is the appearance in magnetotransport of equally spaced Landau levels crossing the Fermi level, instead of a single chiral level as in Weyl semimetals [13,14]. To investigate the magnetotransport properties of both TNP and NTNP phases, the Landau-level spectra are calculated by performing a Peierls substitution in a $\boldsymbol{k}\cdot\boldsymbol{p}$ model. First, a simple $\boldsymbol{k}\cdot\boldsymbol{p}$ model in the absence of SOC is constructed with a minimal basis set of $|p_x\rangle$, $|p_y\rangle$, and $|d_{xy}\rangle$ orbitals (in that order) respecting the D_{4h} point symmetry around the X_3 point. Our model includes a pair of TNPs in contrast with the previous study focusing on a single TNP [14]. By applying symmetry constraints and keeping terms up to quadratic order, a $\boldsymbol{k}\cdot\boldsymbol{p}$ model for a pair of TNPs is obtained as

$$\mathcal{H}(\boldsymbol{k}) = \begin{pmatrix} h_{11}(\boldsymbol{k}) & b_2k_xk_y & c_2k_y \\ b_2k_xk_y & h_{22}(\boldsymbol{k}) & c_2k_x \\ c_2k_y & c_2k_x & h_{33}(\boldsymbol{k}) \end{pmatrix}, \tag{2}$$

where $\boldsymbol{k}$ is a relative wave vector from the X_3 point and the diagonal terms are

$$\begin{aligned} h_{11}(\boldsymbol{k}) &= a_0 + a_1k_x^2 + a_2k_y^2 + a_3k_z^2, \\ h_{22}(\boldsymbol{k}) &= a_0 + a_2k_x^2 + a_1k_y^2 + a_3k_z^2, \\ h_{33}(\boldsymbol{k}) &= d_0 + d_1\left(k_x^2 + k_y^2\right) + d_3k_z^2. \end{aligned} \tag{3}$$

Figures 10(a) and 10(e) show the band structure calculated with parameters chosen to resemble the first-principles results. Assuming an external magnetic field along the [001] direction, the k_x and k_y terms are replaced by Landau-level ladder operators according to

$$\begin{aligned} \pi_x &= k_x - eA_x \rightarrow \frac{1}{\sqrt{2}l_B}(\hat{a}^+ + \hat{a}), \\ \pi_y &= k_y - eA_y \rightarrow \frac{1}{i\sqrt{2}l_B}(\hat{a}^+ - \hat{a}), \end{aligned} \tag{4}$$

where A_i is the vector potential, $l_B = \sqrt{\hbar/eB}$ is the magnetic length, and $\hat{a}|n\rangle = \sqrt{n}|n-1\rangle$, and $\hat{a}^+|n\rangle = \sqrt{n+1}|n+1\rangle$ are the lowering and raising operators, respectively, acting on the nth Landau level.

The Landau-level spectra are then calculated with a finite number of Landau levels in the basis. The result for the TNP phase is shown in Fig. 10(b). The zeroth Landau level, the outermost of the parabolic ones, connects valence and conduction Landau bands. In contrast to Weyl semimetals, additional Landau levels appear in the vicinity of the zeroth Landau level with a gradual shift to lower energy, forming a dense parabolic spectrum [14]. The small downward shift between subsequent Landau levels is determined by the negative dispersion of band 6 shown in Figs. 1(c)–1(e) and 1(h), whose parabolic dispersion along the direction normal to the applied magnetic field allows higher Landau levels at lower energy. This behavior is consistent with the results of a previous study [14] after taking into account that the dispersion was positive there, so that the Landau levels shifted upwards instead.

In the case of the NTNP phase, the SOC together with the [100]-oriented magnetization lowers the symmetry considerably, but the $C_2^{[100]}$ and $\sigma_{[100]}$ symmetries survive. The result is that the modified symmetry allows new terms in the $\boldsymbol{k}\cdot\boldsymbol{p}$ model of the form k_yk_z in all the diagonal terms, k_xk_z in h_{12}, and k_z in h_{13}.[3] The extra term in h_{13} is relevant to the mass gap of the NTNP.

The Landau-level spectrum of the NTNP phase is shown in Fig. 10(c). This also exhibits a zeroth Landau level connecting valence and conduction Landau bands, spreading downward as in the TNP phase. Although the NTNP phase gives similar results to the TNP phase and previous studies, this specific calculation is not realistic in the sense that the applied orbital magnetic field (along [001]) and the spin magnetization orientation (along [100]) are not parallel. If the spin magnetization aligns with the external field, the NTNP splits into Weyl points as shown in Fig. 10(d), where the upper and lower Weyl points exhibit opposite chirality.

Therefore, we consider a case in which both the external field and magnetization orientation are aligned along the [100] direction by carrying out the ladder-operator replacement on the k_y and k_z terms in the $\boldsymbol{k}\cdot\boldsymbol{p}$ Hamiltonian. Figures 10(f) and 10(g) show the Landau-level spectra along the k_x direction for the TNP and NTNP phases, respectively. In contrast with previous cases [Figs. 10(b)–10(d)], the parabolic spectrum of Landau-level curves now spreads in both directions in energy, and the zeroth Landau level does not appear among them, since there is no longer a band extremum in the 2D momentum space orthogonal to the axis. In this case we find difficulty in converging the calculation with respect to the basis set size, so that our confidence in the accuracy of the calculation is reduced. Nevertheless, the similarity of the magnetotransport properties between the NTNP and TNP phases is clear, implying that half-metallic GdN can serve as a useful platform for investigating the properties of the TNP phase.

IV. SUMMARY

By employing *ab initio* calculations, we have investigated the topological nature of the band crossing points in half-metallic GdN. The emergent triple nodal points in the absence of SOC split into conventional Weyl points when taking the weak SOC into account. Interestingly, some crossing points on the C_4 rotation axis orthogonal to the magnetization direction remain in the nearly degenerate triple nodal point state. These “nearly triple nodal points” induce quantitatively similar surface spectra and transport properties compared with those of true triple nodal points. The transition as a function of magnetization orientation between the nearly triple nodal point and Weyl point phases opens promising opportunities for the manipulation of the rich surface-state structure.

ACKNOWLEDGMENTS

We thank N. Kioussis and P.-Y. Chang for helpful discussions. This work was supported by the National Science Foundation under Grant No. DMR-1408838.

---

[3] The reduced symmetry also implies that some coefficients that were identical in Eqs. (2) and (3) can become different. For example, $h_{11}(k,0,0) = h_{22}(0,k,0)$ is no longer enforced without $C_4^{[001]}$ symmetry. However, such changes are expected to be small and have not been incorporated into the model used in the calculations presented here.

[1] M. Z. Hasan and C. L. Kane, Rev. Mod. Phys. **82**, 3045 (2010).

[2] X.-L. Qi and S.-C. Zhang, Rev. Mod. Phys. **83**, 1057 (2011).

[3] Y. Ando and L. Fu, Annu. Rev. Condens. Matter Phys. **6**, 361 (2015).

[4] J. Wang, B. Lian, and S.-C. Zhang, Phys. Scr. **2015**, 014003 (2015).

[5] B. Bradlyn, L. Elcoro, J. Cano, M. G. Vergniory, Z. Wang, C. Felser, M. I. Aroyo, and B. A. Bernevig, Nature (London) **547**, 298 (2017).

[6] H. Weng, X. Dai, and Z. Fang, J. Phys.: Condens. Matter **28**, 303001 (2016).

[7] C.-K. Chiu, J. C. Y. Teo, A. P. Schnyder, and S. Ryu, Rev. Mod. Phys. **88**, 035005 (2016).

[8] A. Bansil, H. Lin, and T. Das, Rev. Mod. Phys. **88**, 021004 (2016).

[9] T. T. Heikkilä and G. E. Volovik, New J. Phys. **17**, 093019 (2015).

[10] T. Hyart and T. T. Heikkilä, Phys. Rev. B **93**, 235147 (2016).

[11] B. Bradlyn, J. Cano, Z. Wang, M. G. Vergniory, C. Felser, R. J. Cava, and B. A. Bernevig, Science **353**, aaf5037 (2016).

[12] H. Weng, C. Fang, Z. Fang, and X. Dai, Phys. Rev. B **93**, 241202 (2016).

[13] Z. Zhu, G. W. Winkler, Q. S. Wu, J. Li, and A. A. Soluyanov, Phys. Rev. X **6**, 031003 (2016).

[14] G. Chang, S.-Y. Xu, S.-M. Huang, D. S. Sanchez, C.-H. Hsu, G. Bian, Z.-M. Yu, I. Belopolski, N. Alidoust, H. Zheng, T.-R. Chang, H.-T. Jeng, S. A. Yang, T. Neupert, H. Lin, and M. Z. Hasan, Sci. Rep. **7**, 1688 (2017).

[15] H. Yang, J. Yu, S. S. P. Parkin, C. Felser, C.-X. Liu, and B. Yan, Phys. Rev. Lett. **119**, 136401 (2017).

[16] C.-G. Duan, R. F. Sabirianov, W. N. Mei, P. A. Dowben, S. S. Jaswal, and E. Y. Tsymbal, J. Phys.: Condens. Matter **19**, 315220 (2007).

[17] F. Natali, B. Ruck, N. Plank, H. Trodahl, S. Granville, C. Meyer, and W. Lambrecht, Prog. Mater. Sci. **58**, 1316 (2013).

[18] C. M. Aerts, P. Strange, M. Horne, W. M. Temmerman, Z. Szotek, and A. Svane, Phys. Rev. B **69**, 045115 (2004).

[19] M. Horne, P. Strange, W. M. Temmerman, Z. Szotek, A. Svane, and H. Winter, J. Phys.: Condens. Matter **16**, 5061 (2004).

[20] Z. Szotek, W. M. Temmerman, A. Svane, L. Petit, P. Strange, G. M. Stocks, D. Ködderitzsch, W. Hergert, and H. Winter, J. Phys.: Condens. Matter **16**, S5587 (2004).

[21] D. X. Li, Y. Haga, H. Shida, T. Suzuki, Y. S. Kwon, and G. Kido, J. Phys.: Condens. Matter **9**, 10777 (1997).

[22] Z. Li, J. Kim, N. Kioussis, S.-Y. Ning, H. Su, T. Iitaka, T. Tohyama, X. Yang, and J.-X. Zhang, Phys. Rev. B **92**, 201303 (2015).

[23] G. Xu, H. Weng, Z. Wang, X. Dai, and Z. Fang, Phys. Rev. Lett. **107**, 186806 (2011).

[24] P. Wachter and E. Kaldis, Solid State Commun. **34**, 241 (1980).

[25] C.-G. Duan, R. F. Sabiryanov, J. Liu, W. N. Mei, P. A. Dowben, and J. R. Hardy, Phys. Rev. Lett. **94**, 237201 (2005).

[26] W. R. L. Lambrecht, Phys. Rev. B **62**, 13538 (2000).

[27] F. Leuenberger, A. Parge, W. Felsch, K. Fauth, and M. Hessler, Phys. Rev. B **72**, 014427 (2005).

[28] S. Granville, B. J. Ruck, F. Budde, A. Koo, D. J. Pringle, F. Kuchler, A. R. H. Preston, D. H. Housden, N. Lund, A. Bittar, G. V. M. Williams, and H. J. Trodahl, Phys. Rev. B **73**, 235335 (2006).

[29] H. J. Trodahl, A. R. H. Preston, J. Zhong, B. J. Ruck, N. M. Strickland, C. Mitra, and W. R. L. Lambrecht, Phys. Rev. B **76**, 085211 (2007).

[30] P. Wachter, Results Phys. **2**, 90 (2012).

[31] H. Yoshitomi, S. Kitayama, T. Kita, O. Wada, M. Fujisawa, H. Ohta, and T. Sakurai, Phys. Rev. B **83**, 155202 (2011).

[32] H. Yoshitomi, R. Vidyasagar, S. Kitayama, T. Kita, H. Ohta, S. Okubo, Y. Fukuoka, and T. Sakurai, Appl. Phys. Lett. **101**, 072403 (2012).

[33] T. Kagawa and H. Raebiger, Phys. Rev. Appl. **2**, 054009 (2014).

[34] G. Kresse and J. Furthmüller, Phys. Rev. B **54**, 11169 (1996).

[35] G. Kresse and J. Furthmüller, Comput. Mater. Sci. **6**, 15 (1996).

[36] A. A. Mostofi, J. R. Yates, G. Pizzi, Y.-S. Lee, I. Souza, D. Vanderbilt, and N. Marzari, Comput. Phys. Commun. **185**, 2309 (2014).

[37] P. E. Blöchl, Phys. Rev. B **50**, 17953 (1994).

[38] G. Kresse and D. Joubert, Phys. Rev. B **59**, 1758 (1999).

[39] J. P. Perdew, K. Burke, and M. Ernzerhof, Phys. Rev. Lett. **77**, 3865 (1996).

[40] M. P. L. Sancho, J. M. L. Sancho, and J. Rubio, J. Phys. F: Met. Phys. **15**, 851 (1985).

[41] T. Ozaki, K. Nishio, and H. Kino, Phys. Rev. B **81**, 035116 (2010).

[42] J.-W. Rhim and Y. B. Kim, Phys. Rev. B **92**, 045126 (2015).

[43] P.-Y. Chang and C.-H. Yee, Phys. Rev. B **96**, 081114 (2017).

[44] T.-T. Zhang, Z.-M. Yu, W. Guo, D. Shi, G. Zhang, and Y. Yao, J. Phys. Chem. Lett. **8**, 5792 (2017).

[45] C. Fang, M. J. Gilbert, X. Dai, and B. A. Bernevig, Phys. Rev. Lett. **108**, 266802 (2012).

[46] S. S. Tsirkin, I. Souza, and D. Vanderbilt, Phys. Rev. B **96**, 045102 (2017).

[47] F. D. M. Haldane, Attachment of surface “Fermi arcs” to the bulk Fermi surface: “Fermi-level plumbing” in topological metals, arXiv:1401.0529.